Highlights

Investigating the uniaxial compressive mechanics of graded polymer foams via *in-situ* synchrotron X-ray microtomography

Paolo Iaccarino, Clément Rey, Lorenzo Miele, Victor Okumko, Mario Scheel, Timm Weitkamp, Henry Proudhon, Ferdinando Auricchio, Ernesto Di Maio, Andrei Constantinescu

- A cylindrical foam with a tailored vertical density gradient was produced via a batch-foaming process.
- *In-situ* synchrotron X-ray microtomography revealed micromechanical deformation mechanisms under compressive loading.
- The tailored graded foam demonstrates distinct energy absorption behavior, outperforming uniform foams.
- The density graded architecture enables precise tuning of collapse band formation and propagation during compression.

Investigating the uniaxial compressive mechanics of graded polymer foams via *in-situ* synchrotron X-ray microtomography

Paolo Iaccarino[a,b,c,*], Clément Rey[d], Lorenzo Miele[b,c], Victor Okumko[e,f], Mario Scheel[e], Timm Weitkamp[e], Henry Proudhon[f], Ferdinando Auricchio[g], Ernesto Di Maio[b,c], Andrei Constantinescu[d,*]

[a]*Scuola Superiore Meridionale, Largo San Marcellino 10, Naples, 80138, Italy*
[b]*Dipartimento di Ingegneria Chimica, dei Materiali e della Produzione Industriale, University of Naples Federico II, P.le Tecchio 80, Naples, 80125, Italy*
[c]*foamlab, University of Naples Federico II, P.le Tecchio 80, Naples, 80125, Italy*
[d]*Laboratoire de Mécanique des Solides, CNRS, École Polytechnique, Institut Polytechnique de Paris, Palaiseau, 91128, France*
[e]*Synchrotron SOLEIL, Saint-Aubin, L'Orme des Merisiers, Départementale 128, 91190, Saint-Aubin, France*
[f]*Paris, PSL University, MAT - Centre des Matériaux, CNRS UMR 7633, BP 87, Evry, 91003, France*
[g]*Dipartimento di Ingegneria Civile e Architettura, University of Pavia, Via Ferrata 3, Pavia, 27100, Italy*

Abstract

Graded polymer foams are emerging as transformative materials for structural applications, outperforming uniform foams due to their spatially tailored density and microstructural features. However, harnessing their full potential requires a deep understanding of how their macroscopic mechanical behavior relates to their complex microstructure evolution. In this study, we elucidate the uniaxial compressive response of graded foams using in-situ synchrotron X-ray microtomography, complemented by comparative experiments on uniform foams of varying densities. Our findings reveal that graded foams exhibit both qualitatively and quantitatively distinct mechanical behavior, driven by unique microscale deformation mechanisms. We evaluate and discuss their superior energy absorption performance and demonstrate how the density profile evolves under increasing macroscopic strain. Notably, the graded architecture enables precise control over the localization and progres-

---

[*] Corresponding author. E-mail: paolo.iaccarino-ssm@unina.it (Paolo Iaccarino); andrei.constantinescu@polytechnique.edu (Andrei Constantinescu).

Preprint submitted to Polymer Testing *October 21, 2025*

sion of densification bands, offering unprecedented design flexibility for advanced structural applications.

Keywords: batch foaming, polypropylene, functionally graded, micromechanics, uniaxial compression

---

1. Introduction

Graded polymer foams—hereafter referred to as graded foams—are rapidly emerging as high-performance alternatives to spatially uniform foams [1]. Unlike their uniform counterparts, graded foams exhibit continuous spatial variations in density and/or microstructural features, such as cell size or wall/strut thickness distributions. It is important to distinguish graded foams from layered foams, which exhibit discrete, step-wise changes in density and microstructure—often in a single direction—and are typically fabricated by gluing or soldering layers of uniform foams [2, 3].

Graded polymer foams exhibit significant potential in energy absorption applications, as they enable the customization of their constitutive behavior, for example, through the design of the density map [4]. In fact, density is the primary factor influencing the mechanical properties of polymer foams [5]. However, the challenges associated with the production of graded foams have limited research primarily to theoretical and/or numerical investigations [6, 7, 8, 9, 10], with only a few recent experimental studies successfully producing graded foams using additive manufacturing [11, 12, 13].

Nevertheless, producing a graded foam using additive manufacturing is not always the optimal choice, as it is challenging to reproduce the statistical features (e.g., cell size, cell orientation distributions) of polymer foams. Furthermore, additive manufacturing processes are typically significantly slower than the conventional gas foaming methods employed in industrial applications. Finally, during additive manufacturing, the strain histories are typically bland. In contrast, in gas foaming methods, the extreme strains and strain rates to which the material is subjected serve as fundamental processing tools for enhancing the performance of the base polymer within the cell walls and struts of the resulting foam.

A technology that overcomes these limitations has been introduced by Trofa et al. [14] to produce graded polymeric foams based on time-varying boundary conditions in gas foaming [14]. This technology can be coupled with mechanical constraints and complex preform geometries and has been demonstrated to efficiently produce graded foams with topologically optimized density maps to fulfill targeted structural requirements [1].

To effectively design the density map, a thorough understanding of the micromechanical phenomena underlying macroscopic mechanical behavior is essential. To the best of our knowledge, both the micromechanics and macromechanics of graded foams remain largely unexplored.

Microtomography (µCT) has been widely utilized as a tool to characterize the microstructure of uniform polymer foams *per se* [15, 16], but only a limited number of studies have employed this technique *in-situ* to investigate the relationship between mechanical behavior and micromechanical phenomena [17, 18, 19]. In fact, it is well established that the macroscopic mechanical behavior of foams arises from complex symmetric and asymmetric deformation micromechanisms, including the bending and elastic or plastic buckling of cell walls and struts [5]. Observing these micromechanisms is, therefore, essential for developing a deeper understanding and for proposing more accurate, physics-based multiscale models to predict their mechanical properties.

Besides laboratory X-ray sources, synchrotron radiation (SR) has proved particularly useful for µCT studies on polymer foams, owing not only to the high intensity of SR X-rays, which enables *in-situ* measurements at high resolution in reasonable time, but also because the degree of spatial coherence of SR gives access to inline phase contrast and thus to drastically increased signal for light elements such as those constituting most polymers [20].

The first uniaxial compression studies via *in-situ* synchrotron microtomography on polymer foams were conducted around the turn of the millennium, just after SR-based µCT (SRµCT) had become available, when Elliott et al. [21] characterized open-cell polyurethane foams by *in-situ* compression SRµCT up to 80% compressive strain. The deformation process was shown to occur homogeneously throughout the foam up to a compressive strain of approximately 6%, where collapsed bands of denser material began to form in correspondence with a dramatic loss of tangent stiffness in the stress-strain curve. Importantly, the authors also observed the formation of a collapse band around a particular foam cell that was significantly larger than its immediate neighbors; however, this was not an isolated buckling transition but rather a cooperative collapse involving an entire layer of connected cells of considerable extent [21]. Youssef et al. [22] conducted *in-situ* uniaxial compression SRµCT measurements up to 20% to analyze the deformation mechanisms in a closed-cell polyurethane (PU) foam and to validate a finite element analysis (FEA) modeling procedure [22]. Their FEA reveals that plastic yielding mechanisms take place at a very early stage of macroscopic deformation: in fact, the first yielding point appears at 0.1% of macroscopic strain, which is still in the apparently linear domain of the macroscopic behavior; moreover, the authors numerically observed that at large macroscopic strain an important part of the foam still behaves elastically [22]. Adrien et al. [23] studied the damage evolution of syntactic foams with different matrices (epoxy, polypropylene (PP), and PU) in confined compression via *in-situ* SRµCT measurements, finding that when the matrix is softer (PP and PU) the damage is homogeneously distributed, while for a stiffer matrix (epoxy) the damage is localized in bands [23]. Roux et al. [24] conducted *in-situ* compression SRµCT measurements on PP bead foams up to 30% strain combined with digital image correlation to reveal the heterogeneity of the strain field at both the cell (microscopic, μm) and bead (mesoscopic, mm) scales [24]. Chai et al. [25] investigated the micromechanics of the struts and walls of a closed-cell polymethacrylimide (PMI) foam under uniaxial compression with *in-situ* SRµCT and digital volume correlation, highlighting the correlation between cell wall buckling and deformation bending for closed-cell foams [25]. In a later work, Chai et al. [26] revealed different types (discrete or spreading) of deformation banding for PMI foams with different densities and concluded that elastic buckling of cell walls dominates cell collapse, and the buckling strength of walls highly depends on their thickness and inclination angles with respect to the loading direction [26].

In conclusion, the integration of uniaxial compression tests and *in-situ* SRµCT has significantly enhanced our understanding of the relationship between microstructure and macroscopic mechanical properties in uniform polymer foams.

Within this framework, the aim of the present work is to unveil the mechanics of graded foams simultaneously at both the microscale and macroscale, thereby enhancing the understanding of the *microstructure-property* relationship in these novel polymer foams. To achieve this goal, we first design and produce a graded foam with a density gradient via batch foaming through the recent technology introduced by Trofa et al. [14] coupled with mechanical constraints. Subsequently, we produce two uniform foams: one with a density comparable to the average density of the graded foam and the other with a lower density - the latter to provide a comparison for the lower density regions of the graded foam. We then investigate the mechanics of these three foams at both the microscale and macroscale simultaneously during uniaxial compression experiments using *in-situ* SRµCT. We study the energy absorption performance of the foams, and we compute their density profiles at different levels of macroscopic strain. Additionally, we report interesting details of the foams microstructure during compression.

The present work is organized as follows: section 2 reports the materials utilized and the procedures employed to produce the graded and uniform foams; section 3 provides information on the experimental setup and the protocol used for the uniaxial compression measurement with *in situ* SRµCT; section 4 presents the analysis of (i) the energy absorption performance, (ii) the density profiles at different levels of macroscopic strain, and (iii) microstructural details during the compression of the foams, along with a discussion of these points; section 5 summarizes the findings of the present work and suggests possible directions for future research. In addition, we report the pseudocode used for the 2D segmentation of the tomographs in the Appendix.

2. Materials and foamed samples production

Polypropylene (PP, code E02ES) with a density of $\rho^{\mathrm{PP}} = 905$ kg/m^3 is provided by Sinopec Zhenhai Refining & Chemical Company (Zhejiang Province, China) in the form of a slab 16 mm thick. The slab is machined into cylindrical preforms of bulk PP using a numerically controlled milling machine (MDX-40, Roland DG Corporation, Hamamatsu-shi, Shizuoka-ken, Japan). Three types of cylindrical preforms are produced, with diameter d and height h: type p-U, with $d = 6.7$ mm and $h = 6.7$ mm, which will be used to produce the uniform (U) foams; type p-ULD, with $d = 5.7$ mm and $h = 5.0$ mm, which will be used to produce the uniform low density (ULD) foams; type p-G, with $d = 10$ mm and $h = 3$ mm, which will be used to produce the graded (G) foams. To produce foams, we used CO_2 (purity 99.99%) as a blowing agent, supplied by SOL S.p.A. (Monza, Italy).

The foaming apparatus is a 0.3 L thermoregulated pressure vessel (model BC-1, High Pressure Equipment Co., Erie, PA, USA). The electrical heater is controlled by a PID thermoregulator (mod. 1850, Gefran S.p.A., Provaglio d'Iseo, Brescia, Italy), which takes as input the temperature of the heating jacket by using a type J thermocouple. The temperature of the sample inside the vessel is measured using a Pt100 temperature sensor (Gefran S.p.A., Provaglio d'Iseo, Brescia, Italy). A pressure transducer (model TK, Gefran S.p.A., Provaglio d'Iseo, Brescia, Italy) is used to measure pressure during the saturation step. The pressure discharge system consists of a discharge ball valve (model 15-71 NFB, High Pressure Equipment Co., Erie, PA, USA) and an electromechanical actuator (model 15-72 NFB TSR 8, High Pressure Equipment Co., Erie, PA, USA). The pressure drop rate (PDR) is measured by a programmable logic controller (SIMATIC S7-1200 CPU, Siemens, Munich, Germany) with a sampling rate $\tau_m = 1$ ms, following the procedure proposed by Miele et al. [27]. A more detailed description of the experimental setup and of the described configuration can be found in Iaccarino et al. [28].

The foams are produced as illustrated in Figure 1 and described in the following.

All the preforms are placed in the center of same cylindrical aluminum molds (to give foamed samples of same final geometry) with a diameter of 10 mm and a height of 10 mm. The mold is then inserted into the pressure vessel, and the temperature is increased to 144°C under vacuum conditions. Once the temperature is reached, the pressure of CO_2 is raised to 130 bar and maintained constant for a sorption time, t_s, which depends on the preform type: for types p-U and p-ULD, $t_s = 2700$ s, while for type p-G, $t_s = 450$ s. Subsequently, the pressure is released such that PDR = 500 bar/s, allowing the preforms to expand while being constrained by the mold, thereby producing the U, ULD, and G foams, respectively. An illustrative video of the preforms expansion is provided in Media 1.

Purposely, for the p-G preform 450 s are not sufficient to achieve a uniform (equilibrium) CO_2 concentration profile throughout the preform, and at the pressure release it expands with a designed density gradient and microstructural feature gradients arising from the non-equilibrium CO_2 concentration profile.

To measure the density (ρ_f) of the G, U, and ULD foams, we apply the buoyancy method along with the following equation:

$$\rho_f = \frac{m_a}{m_a - m_w}(\rho_w - \rho_a) + \rho_a \ , \tag{1}$$

where m_a is the weight of the foam in air, m_w is the weight of the foam in water, ρ_a is the density of air, and ρ_w is the density of water. At room temperature (23 ± 2°C), $\rho_a = 1.20$ kg/m^3 and $\rho_w = 997.5$ kg/m^3 [29]. The values m_a and m_w are measured using an analytical balance (model MS Semi-Micro, Mettler Toledo, Milan, Italy).

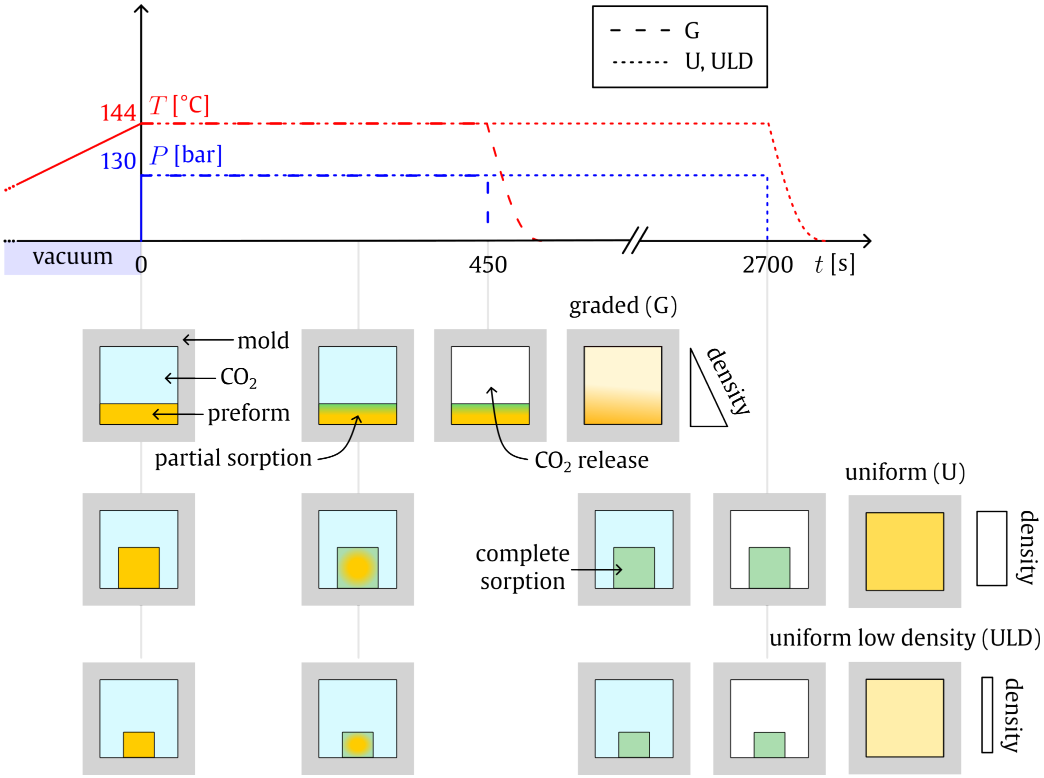

Figure 1: Schematic of the production process of the graded (G), uniform (U) and uniform low density (ULD) foams used in this work. The different preforms are placed in identical cylindrical molds. The pressure vessel is then heated to a constant temperature of 144 °C under vacuum conditions. Once such a temperature is reached, a constant pressure of 130 bar CO_2 is applied. In the case of the preform p-G, the pressure is released after a sorption time of 450 s. Since the preform is only partially saturated with CO_2, it results in a foam with a density graded profile. In the case of the preforms p-U and p-ULD, the sorption step lasts 2700 s, allowing full CO_2 saturation of the preforms before pressure release, and the production of foams with uniform densities (U and ULD foams, respectively).

3. Synchrotron measurement and data analysis

SRµCT experiments are conducted at the ANATOMIX beamline [30, 31] at the SOLEIL synchrotron radiation facility [32]. The experimental setup is illustrated in Figure 2.

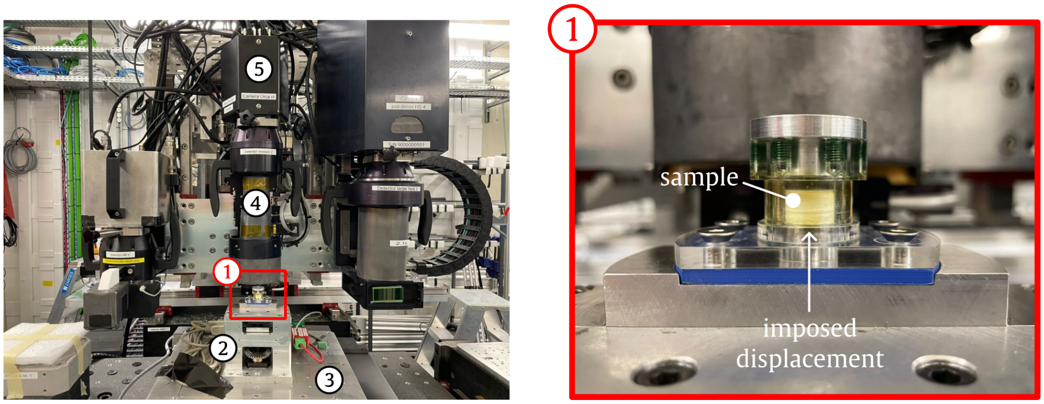

Figure 2: Experimental setup at the ANATOMIX beamline [31] equipped with the uniaxial testing machine “Bulky” [33]. ① (zoomed in on the right) upper part of Bulky: for the compression testing, the foam sample is placed in a polymethyl methacrylate tube (which is transparent to X-rays) and the displacement is then imposed from the bottom [33]; ② lower part of Bulky; ③ rotating base; ④ detector optics; ⑤ camera.

With an electron current of 500 mA in the SOLEIL storage ring and the ANATOMIX undulator X-ray source set to a magnetic gap of 6.4 mm, the polychromatic X-ray beam passes through a series of gold filters with a total thickness of 26 µm. The detector is an indirect system consisting of a single-crystal scintillator screen (cerium-doped lutetium aluminum garnet, supplier: Crytur, Turnov, Czech Republic), visible-light microscope optics (objective: Mitutoyo M PLAN APO 5x / NA0.14) and a scientific-grade CMOS camera (Hamamatsu model Orca Flash 4.0 V3), resulting in an effective pixel size of 1.3 µm and a field of view of 2.6 mm width and height. The exposure time for each projection radiography frame is set to 70 ms. The propagation distance between the tomography rotation axis and the scintillator was 60 mm. Tomography scans are taken with a continuous rotation and 2000 projection angles over 180 degrees; the total time for each scan is around 3 minutes. Tomographic reconstruction is performed using the standard data processing pipeline at the beamline, based on a Python script for pre-processing [34] and the PyHST2 program [35] as the backend, using a Paganin filter with a kernel length of 25 pixels.

Uniaxial compression experiments are performed using the mechanical testing device "Bulky", introduced by Pelerin et al. [33] and specifically developed for SRµCT. The device consisted of a lower moving grip attached to an in-line crosshead and an upper stationary grip, allowing for precise displacement controlled loading [33]. For these experiments, a 500 lb load cell was installed on the lower part of the frame, as depicted in Figure 2, and connected to a dedicated conditioner, with alignment ensured through sample grips to provide reliable force monitoring.

Since all samples are 10 mm high, multiple scans are performed per sample (ranging from three to five, depending on the nominal strain level) in a column-wise fashion. Subsequent scans are conducted with an overlap of 125 voxels height (~ 0.16 mm) to enable reliable reconstruction of the entire height of the sample.

Each loading/unloading phase is conducted with a constant velocity of 60 μm/min. Due to the viscoelastic nature of the base material, investigated in [36], the resulting foam is also viscoelastic. Hence, after each loading/unloading phase, we allow the sample to relax and recover prior to acquisition. Since the time to relax and recover depends on the current engineering strain [37], the force-time curve is acquired and visualized in real-time to determine whether the material is sufficiently relaxed before initiating the acquisition. The duration of each experiment is approximately 10 hours. In such a duration, considering that we do not irradiate the sample during relaxation/recovery steps, we assume that the effect of the X-ray radiation on the microstructure and mechanical properties of the foam is negligible [38].

Due to the complexity and length of each test, we tested one sample per type. With preliminary microscopy tests, we ensure that each of the samples was fully representative, in terms of density map and microstructural features, of the type of foams produced for this work. The densities of the tested G, U, and ULD foams were measured to be 342 kg/m^3, 302 kg/m^3, and 140 kg/m^3, respectively.

The sequence of strain steps is reported in Table 1 for all samples.

Data analysis is performed using the software Fiji [39] and Python. For each level of strain, virtual slices of the samples, parallel to the vertical axis, are extracted from the tomography data after stacking the volumes obtained in each sub-scan of the respective sample on top of one another using Fiji. The density profile is then computed as follows. First, a segmentation algorithm in Python (reported in the Appendix) is applied to binarize the

strain step [-] **sample**	0%	0.5%	1%	1.5%	5%	10%	5% (u)	20%	10% (u)	40%	20% (u)	50%	40% (u)	0% (u)
G	X		X	X	X	X	X	X	X	X	X	X		X
U	X	X		X	X	X	X	X	X	X	X	X		X
ULD	X	X	X	X	X	X	X	X	X	X	X	X	X	X

Table 1: Strain steps adopted for G, U and ULD foams in the uniaxial compression test. The (u) means that it is an unloading phase which starts from the previous strain step. An empty space indicates that the test was not performed under this condition.

vertical sections. Thus, for each row—associated with a given height of the sample—we denote the pixel values after binarization as $p_i \in \{0, 1\}$ such that $i = 1, ..., N$, where $N = 1950$ is the number of columns. The density ρ_j of row $j \in [1, M]$ (where M is the number of rows, which varies depending on the level of nominal strain) is computed as follows:

$$\rho_j = \frac{\rho^{\mathrm{PP}}}{N} \sum_{i=1}^{N} p_i \ . \tag{2}$$

Then, we obtain the smoothed value of ρ_j, $\tilde{\rho}_j$, by applying a moving average centered on ρ_j with a window size of 200 pixels (which corresponds to ~ 253 μm). To perform such a smoothing operation, we use the function *uniform_filter1d* implemented in the SciPy Python library [40] with the default *reflect* option at the boundaries. This indicates that when $j \in [0, 100] \cup [M - 100, M]$ (up to ~ 127 μm from the boundaries) $\tilde{\rho}_j$ values are not fully reliable.

4. Results and Discussion

The results of the uniaxial compression tests of the G, U, and ULD foams are presented in Figure 3.

From Figure 3(a), it can be inferred that the macroscopic compressive mechanical behavior of the G foam differs qualitatively and quantitatively from that of the uniform foams, as evidenced by Figures 3(b) and 3(c) and reported in the literature [5]. As described above, tests are conducted under loading (solid thick lines) and unloading (dashed thin lines) conditions; however, in this work, we will only consider the loading portion of the curve, while the unloading curves and the relaxed foam configurations will be the focus of a forthcoming paper. The loading curves highlight a major feature of the G foam: the absence of a plateau stress, which is conversely evident

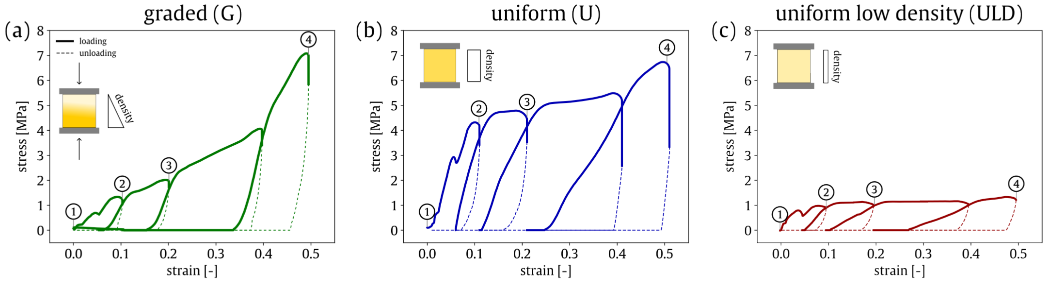

Figure 3: Macroscopic compressive mechanical behavior of (a) the graded, (b) uniform and (c) uniform low density foams. The solid thick segments represents the loading curves, while the dashed thin ones the unloading curves. The circled numbers are referred to specific levels of strain (0%, 10%, 20% and 50%) of the vertical sections that will be analyzed in Figures 5, 6, and 7.

in the U and ULD foams. As it will be shown in Figure 5, this behavior can be attributed to the specific porous architecture at the microscale.

To further highlight the differences in macroscopic mechanical behavior, it is important to study and compare the energy absorption performance of the foams. Specifically, we compute the absorbed energy per unit volume (W) from the loading curves presented in Figure 3, as follows:

$$W = \int_0^{\epsilon} \sigma(e) de \quad , \tag{3}$$

and the efficiency, E [41],

$$E = \frac{\int_0^{\epsilon} \sigma(e) de}{\sigma(\epsilon)} \quad . \tag{4}$$

The absorbed energy and efficiency curves are presented in Figures 4(a) and (b) as functions of stress. The color gradient of each curve corresponds to the strain levels reported in the legend.

Even observing such curves, the difference between the uniform foams and the graded one is straightforward. In the case of U and ULD, there is virtually a single stress value at which energy is absorbed ($\sim$ 5 MPa for the U foam and $\sim$ 1 MPa for the ULD foam), which corresponds to the plateau stress dictated by the density. Conversely, G foams are characterized by a broad spectrum of stress values over which energy can be absorbed, ranging from 0.5 to 7 MPa. Similar arguments can be utilized to illustrate

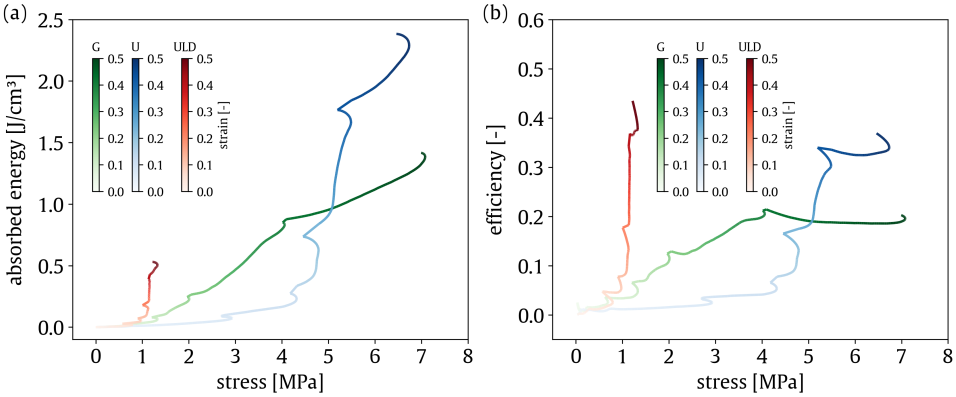

Figure 4: Energy absorption performance of the G, U and ULD foams with respect to stress. Strain is also reported using proper colorbars. (a) Absorbed energy (Eq. 3). (b) Efficiency (Eq. 4).

the differences observed in the efficiency curves. We can anticipate that a graded foam is particularly advantageous when energy has to be absorbed in a real-life scenario of impact absorption, as the stress level is not known *a priori*. The absorbed energy and efficiency curves shown in Figures 4(a) and (b) qualitatively align with the theoretical results presented by Koohbor and Kidane [4]; however, the quantitative theoretical modeling of the observed behavior of the graded foams will be the focus of a forthcoming paper.

The macroscopic mechanical results can be better understood in light of the microstructural features, which are depicted in Figures 5, 6, 7.

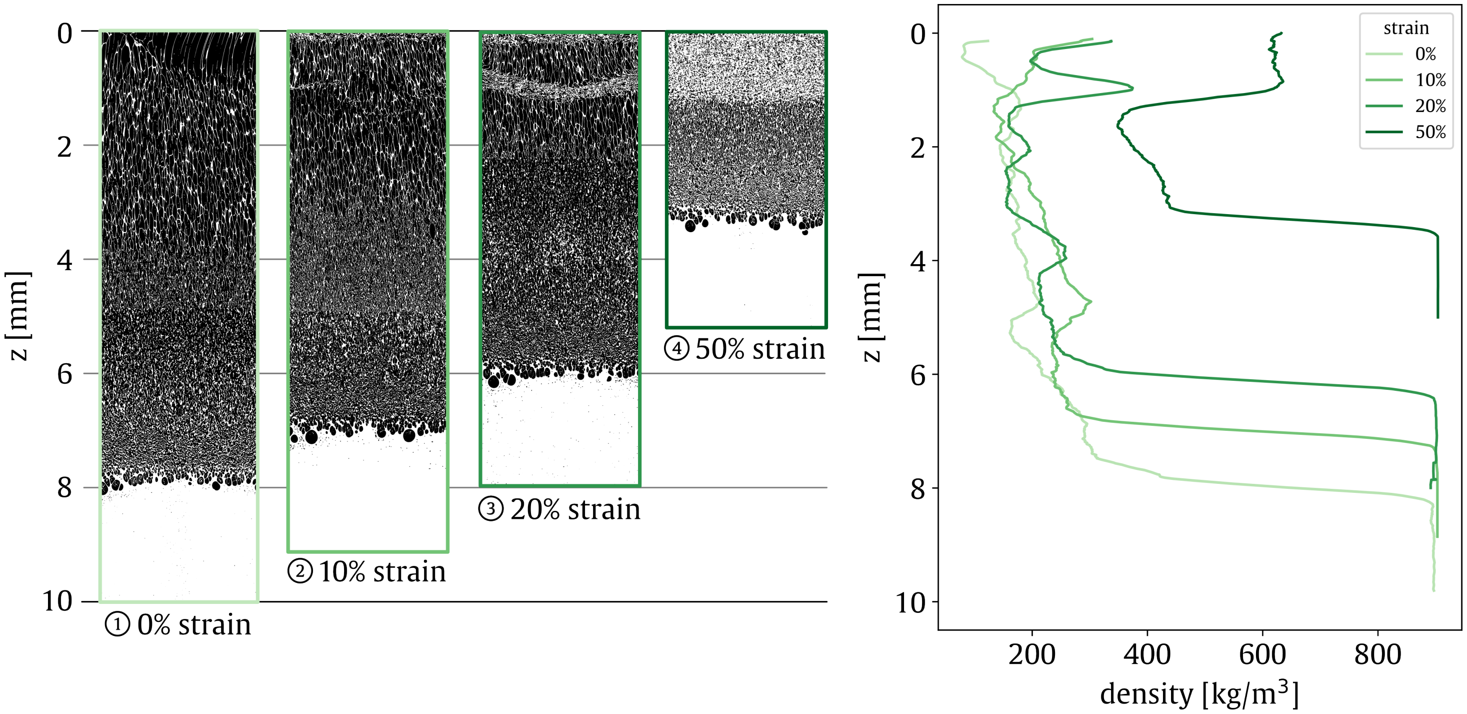

Figure 5: On the left, the binarized vertical sections of the graded foam at 0% (reference configuration), 10%, 20% and 50% strain. White: material (PP), black: pore space. Underlaid, a grid with the z-coordinate is in correspondence with the figure on the right, which reports the density profile (computed as described in section 3) as a function of the z-coordinate. The levels of strain are in correspondence with the stress levels of Figure 3(a) trough the circled numbers.

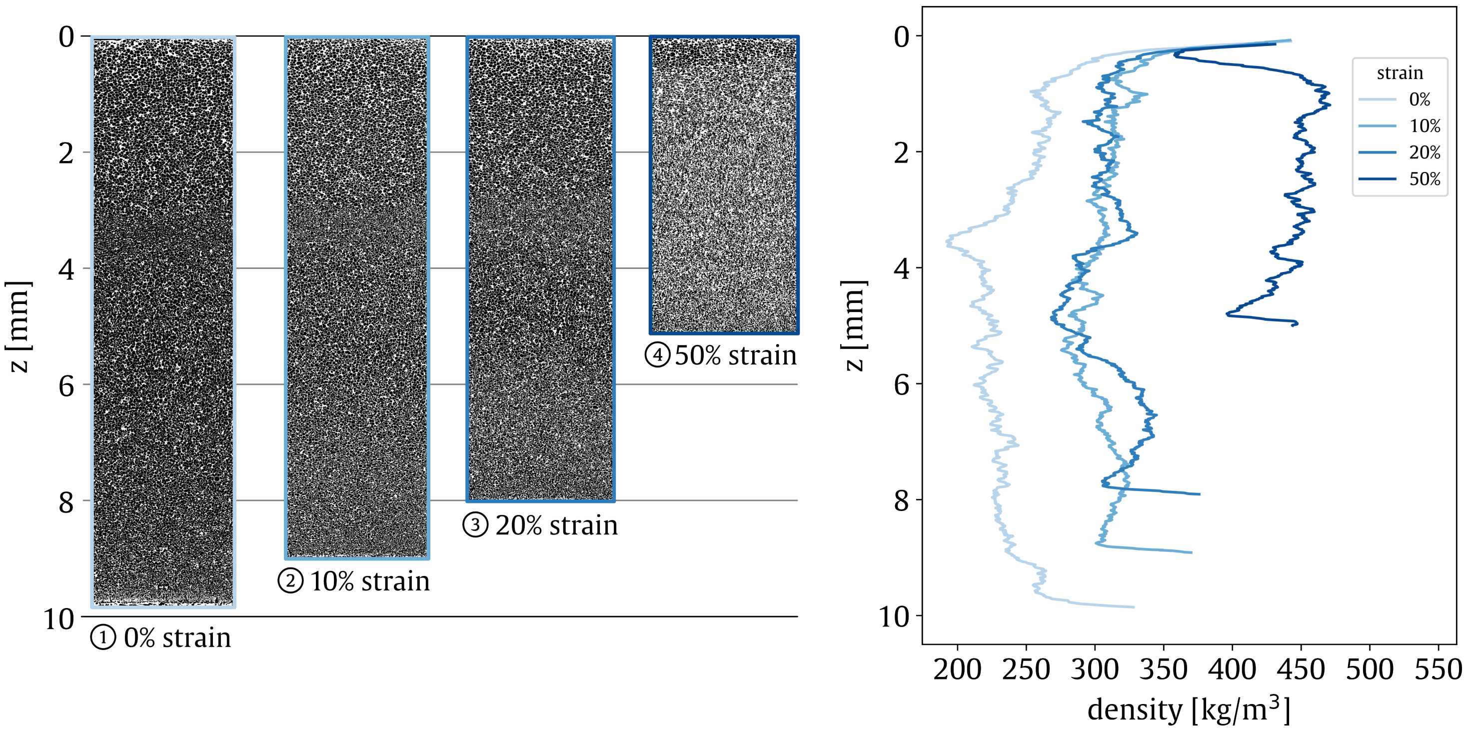

Figure 6: On the left, the binarized vertical sections of the uniform foam at 0% (reference configuration), 10%, 20% and 50% strain. White: material(PP), black: pore space. Underlaid, a grid with the z-coordinate is in correspondence with the figure on the right, which reports the density profile (computed as described in section 3) as a function of the z-coordinate and of the strain. The levels of strain are in correspondence with the stress levels of Figure 3(b) trough the circled numbers.

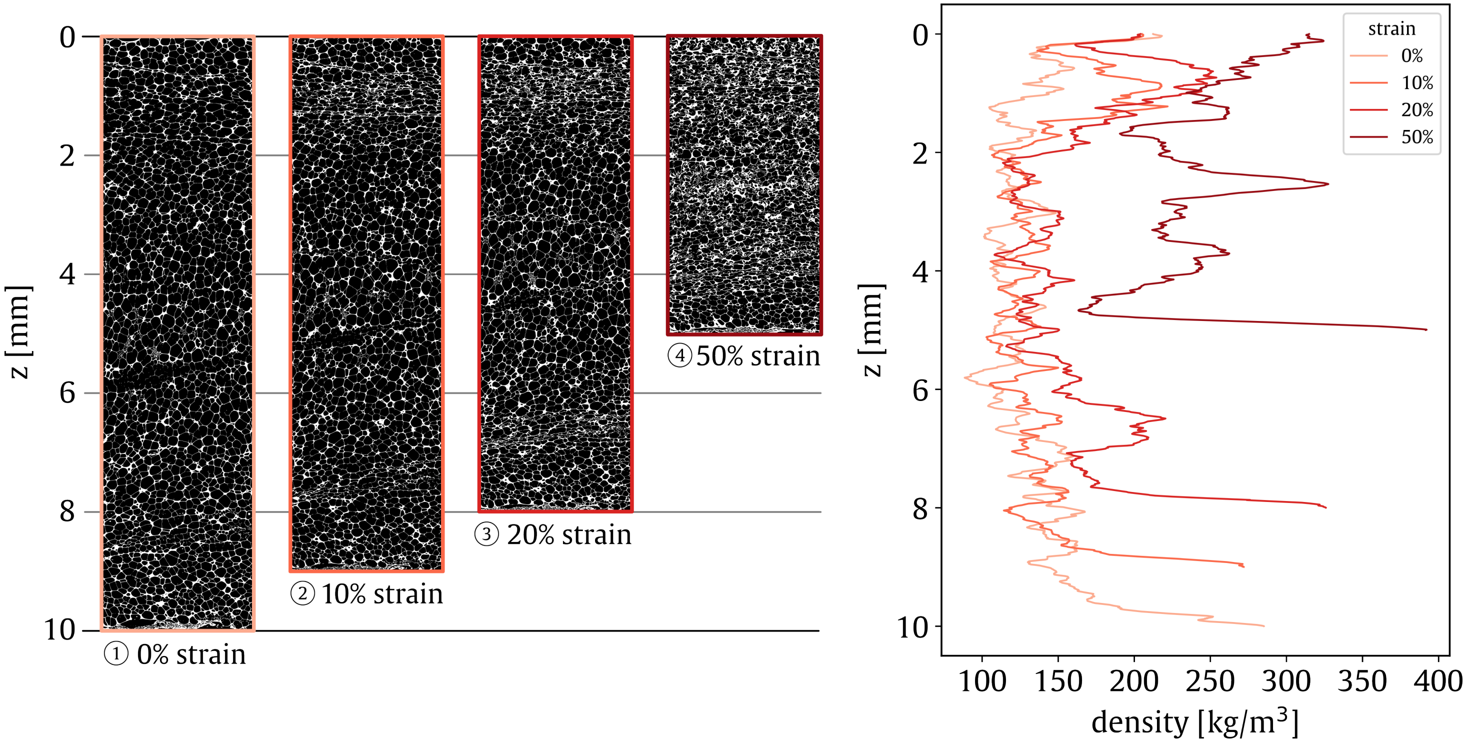

Figure 7: On the left, the binarized vertical sections of the uniform low density foam at 0% (reference configuration), 10%, 20% and 50% strain. White: material (PP), black: pore space. Underlaid, a grid with the z-coordinate is in correspondence with the figure on the right, which reports the density profile (computed as described in section 3) as a function of the z-coordinate and of the strain. The levels of strain are in correspondence with the stress levels of Figure 3(c) trough the circled numbers.

The vertical sections of the G foam at four selected strain levels (0%, 10%, 20%, and 50%) are shown in Figure 5, together with the corresponding density profiles ($\tilde{\rho}_j$ as a function of the z-coordinate, computed as described in Section 3). In the reference configuration (i.e., 0% strain), a clear density gradient is observable, accompanied by both a microstructural anisotropy and a cell size gradient of the cells, arising from the preferential expansion direction during graded foam production. Upon compression, collapse bands develop predominantly in the upper part of the sample, which corresponds to the region of lowest density. At 50% strain, it is evident that densification progresses from the top toward the bottom of the specimen, i.e., from the low-density to the high-density region. This gradient-driven collapse is consistent with the gradual stress increase observed in Figure 3(a). As expected, this behavior contrasts with the compressive response of the U and ULD foams. For proper comparison, Figures 6 and 7 present the reference and deformed configurations of the U and ULD foams at the same strain levels, along with their respective density profiles. In the U foam, densification occurs in a nearly homogeneous manner across the sample height, as evidenced by the evolution of its density profiles. In contrast, the ULD foam exhibits highly localized deformation, with pronounced density peaks emerging during compression. Figure 8 further highlights these mechanisms: while the U foam maintains a relatively uniform deformation at low strain, the ULD foam already shows severe local displacements and distortions as early as 10% strain.

To further investigate the micromechanisms underlying the formation of densification regions, we present in Figure 9 details of the compression bands observed at strains of up to 10% in the G and ULD foams.

In the G foam, at a nominal strain of 1.5%, a collective buckling of the most elongated cells in the low-density region can be observed, while the underlying cells remain almost undeformed. As the strain increases, the deformation of these elongated cells becomes progressively more severe, whereas the onset of buckling in the lower cells is only noticeable at around 10% nominal strain. This indicates a pronounced strain localization within the low-density portion of the graded foam. This observation is consistent with the right panel of Figure 9, which highlights the collapse of a specific region in the ULD foam. This region, characterized by a lower local density (thinner struts and walls), is mechanically weaker and, therefore, less capable of sustaining loads compared to its surroundings. Consequently, structural collapse initiates in this localized low-density zone, giving rise to denser bands

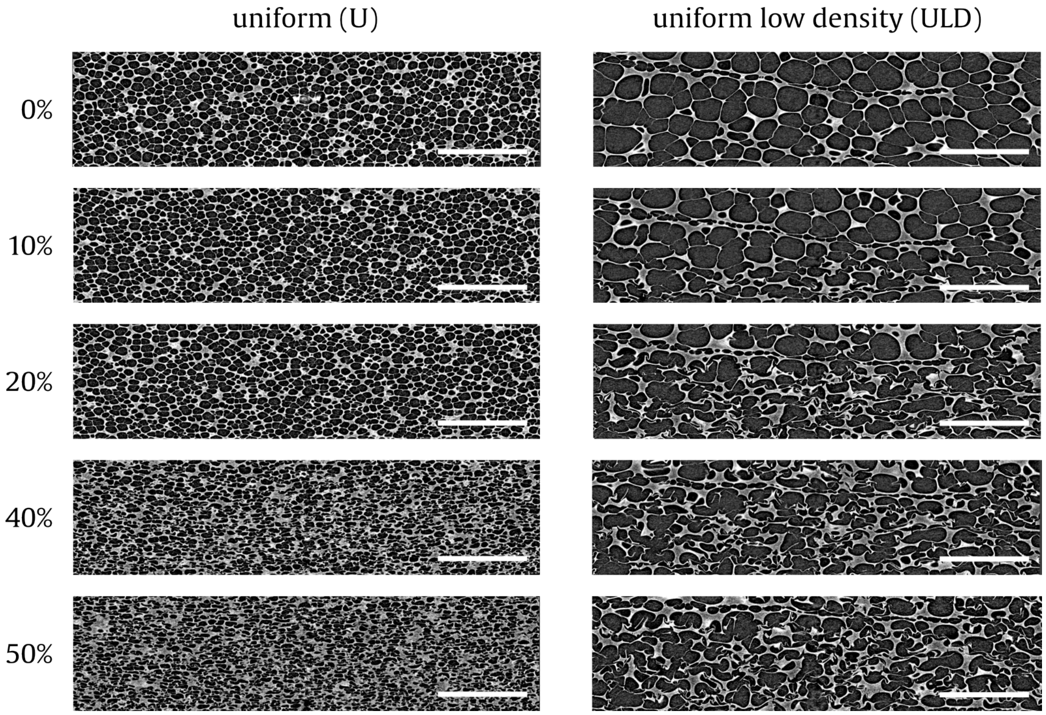

Figure 8: Details of the progressive deformation of U (left) and ULD (right) foams. White bar is 500 μm.

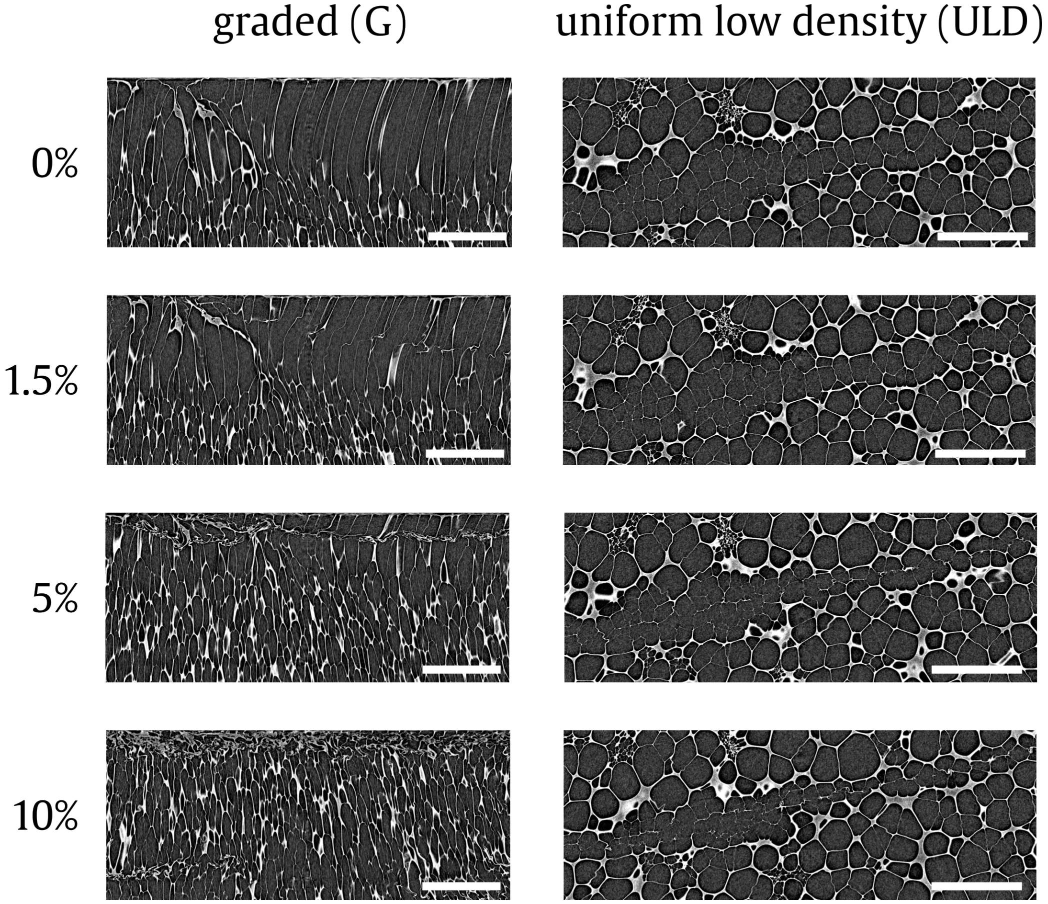

Figure 9: Details of the collapse bands in the G foam (left) and the ULD foam (right) as a function of the nominal strain of the sample. White bar is 500 μm.

in the same region. This behavior aligns with the previous findings of Elliott et al. [21].

5. Conclusion and perspectives

Recent advances in foaming technologies have enabled the production of novel graded foams, which exhibit remarkable properties, particularly in energy absorption. Nevertheless, the relationship between their microstructure and macroscopic mechanical behavior remains poorly understood. To address this gap, we design and fabricate a graded foam with a unidirectional density gradient and investigate its uniaxial compressive behavior via *in-situ* SRµCT. For proper comparison, we also investigate the mechanical response of two uniform foams produced for this purpose. In agreement with theoretical predictions from the literature, the graded foam displays markedly different macroscopic mechanical behavior compared to uniform foams, as reflected in the peculiar shape of its energy absorption (or efficiency) versus stress curve. By computing density profiles as a function of nominal macroscopic strain, we show that this behavior arises from the progressive collapse of the microstructure, which is guided by the density gradient. In contrast, the uniform foams exhibit either nearly homogeneous compression or localized collapse bands, both of which lead to the well-established macroscopic response typical of standard commercial foams. These findings highlight the potential of graded foams for tailored energy absorption applications, as the collapse process can be deliberately guided through density gradation.

To further advance understanding in this field, future efforts should focus on several directions. For example, more efficient segmentation algorithms must be developed to account for the sharp morphological variations present in graded foams. Such tools would enable the quantitative study of statistical microstructural parameters and their evolution under increasing strain. In addition, coupling the analysis of relaxed foam configurations with the relaxation behavior of both the foams and their base materials could provide new insights into the time-dependent mechanisms governing deformation at the microscale.

CRediT authorship contribution statement

Paolo Iaccarino: conceptualization, methodology, software, validation, formal analysis, investigation, data curation, writing - original draft, writing

- review & editing, visualization, project administration. **Clément Rey**: software, investigation, data curation, visualization, writing - original draft. **Lorenzo Miele**: investigation, data curation, visualization, writing - review & editing. **Victor Okumko**: investigation, writing - review & editing. **Mario Scheel**: methodology, software, validation, formal analysis, data curation, resources, writing - review & editing, supervision. **Timm Weitkamp**: methodology, validation, resources, writing - review & editing, supervision. **Henry Proudhon**: methodology, software, resources, writing - review & editing, supervision, funding acquisition. **Ferdinando Auricchio**: conceptualization, methodology, validation, resources, writing - review & editing, visualization, supervision, funding acquisition. **Ernesto Di Maio**: conceptualization, methodology, validation, resources, writing - original draft, writing - review & editing, visualization, supervision, funding acquisition. **Andrei Constantinescu**: conceptualization, methodology, software, formal analysis, investigation, resources, data curation, writing - original draft, writing - review & editing, visualization, supervision, project administration, funding acquisition.

Declaration of competing interest

The authors declare that they have no known competing financial interests or personal relationships with any individuals or organizations that could be perceived to influence the work reported in this paper.

Acknowledgments

The authors thank Synchrotron SOLEIL for the ANATOMIX beamline time (proposal n°20241288, *Investigating the micromechanics of graded polymer foams*, main proposer: Paolo Iaccarino). ANATOMIX is an Equipment of Excellence (EQUIPEX) funded by the *Investments for the Future* program of the ANR, project *NanoimagesX*, grant no. ANR-11-EQPX-0031. The authors also thank Andrew King and Guillaume Daniel (Synchrotron SOLEIL) for assistance in the installation of Bulky and Pasquale Strazzullo (University of Naples Federico II) for the help in realizing the Media 1 for the visualization of the preforms expansion.

Appendix: Pseudocode for 2D Tomography Segmentation Processing

Main Processing Pipeline

Algorithm 1 2D Tomography Segmentation Proccessing Pipeline

```
Require: 2D volume $V \in \mathbb{R}^{H \times W}$
Ensure: Binary segmented volume $B \in \{0,1\}^{H \times W}$
$V_{enhanced} \leftarrow$ CLAHE_2D($V$)
$V_{filtered} \leftarrow$ GuidedFilter2D($V_{enhanced}$)
$B_{sauvola} \leftarrow$ Sauvola2D($V_{filtered}$)
$B_{kmeans} \leftarrow$ KMeans2D($V_{filtered}$)
$B \leftarrow B_{sauvola} \vee B_{kmeans}$                ▷ Logical OR combination
return $B$
```

2D CLAHE Enhancement

Algorithm 2 Memory-Efficient 2D CLAHE

```
Require: Volume $V$, tile size $(t_y, t_x)$, clip limit $c$, bins $n_{bins}$
Ensure: Enhanced volume $V_{enhanced}$
Normalize $V$ to $[0,1]$
Compute tile grid dimensions: $n_y = \lceil H/t_y \rceil$, $n_x = \lceil W/t_x \rceil$
Initialize histogram grid $G \in \mathbb{R}^{n_y \times n_x \times n_{bins}}$
for each tile $(i,j)$ in grid do
    Extract tile patch $P_{i,j}$ from $V$
    Compute histogram $h$ of $P_{i,j}$
    Clip histogram: $h_{clipped} \leftarrow \min(h, c \cdot |P_{i,j}|)$
    Redistribute excess uniformly across bins
    Compute CDF: $G[i,j] \leftarrow \mathrm{cumsum}(h_{clipped})/\mathrm{sum}(h_{clipped})$
end for
for each batch of slices do
    for each voxel $(y,x)$ in batch do
        Find bin index $b$ for intensity $V[y,x]$
        Compute tile coordinates $(t_y, t_x) = (y \cdot n_y/H, x \cdot n_x/W)$
        $V_{enhanced}[y,x] \leftarrow$ BilinearInterpolate($G[\cdot,\cdot,b], t_y, t_x$)
    end for
end for
return $V_{enhanced}$
```

2D Guided Filter

Algorithm 3 2D Guided Filter

```
Require: Image $I$, radius $r$, regularization $\beta$
Ensure: Filtered image $q$
$\mu_I \leftarrow \textsc{UniformFilter}(I, 2r+1)$                ▷ Local mean
$\mu_{II} \leftarrow \textsc{UniformFilter}(I^2, 2r+1)$           ▷ Local mean of $I^2$
$\sigma_I^2 \leftarrow \mu_{II} - \mu_I^2$                        ▷ Local variance
if $\beta$ is None then
    $\beta \leftarrow \sqrt{\text{percentile}(\sigma_I^2, 1) \cdot \text{percentile}(\sigma_I^2, 99)}$
end if
$a \leftarrow \frac{\sigma_I^2}{\sigma_I^2 + \beta}$              ▷ Filter coefficient
$b \leftarrow (1 - a) \cdot \mu_I$                                ▷ Bias term
$q \leftarrow a \cdot I + b$                                      ▷ Final output
return $q$
```

Multi-Scale Sauvola Thresholding

Algorithm 4 2D Multi-Scale Sauvola Segmentation

```
Require: Image $I$, radius range $R = \{r_1, r_2, \ldots, r_n\}$, parameter $c$, normalization $R_{norm}$
Ensure: Binary image $B_{sauvola}$
Initialize $B_{sauvola} \leftarrow \mathbf{0}$                    ▷ All zeros
Normalize $I$ to $[0, 255]$
for each radius $r \in R$ do
    $\mu \leftarrow \textsc{UniformFilter}(I, 2r+1)$              ▷ Local mean
    $\mu_{sq} \leftarrow \textsc{UniformFilter}(I^2, 2r+1)$       ▷ Local mean of $I^2$
    $\sigma \leftarrow \sqrt{\max(\mu_{sq} - \mu^2, \epsilon)}$   ▷ Local std, $\epsilon = 10^{-5}$
    $T \leftarrow \mu \cdot \left(1 + c \cdot \left(\frac{\sigma}{R_{norm}} - 1\right)\right)$   ▷ Sauvola threshold
    $B_r \leftarrow I > T$                                        ▷ Binary result for radius $r$
    $B_{sauvola} \leftarrow B_{sauvola} \vee B_r$                 ▷ Combine with OR
end for
return $B_{sauvola}$
```

Fast 2D K-Means Clustering

Algorithm 5 Fast 2D K-Means Segmentation

```
Require: Image $I$, number of clusters $k$, sampling ratio $s$
Ensure: Binary image $B_{kmeans}$
Flatten image: $X \leftarrow \text{flatten}(I)$
Sample subset: $X_s \leftarrow \textsc{RandomSample}(X, s \cdot |X|)$
Fit K-means: model $\leftarrow \textsc{MiniBatchKMeans}(k).\text{fit}(X_s)$
Predict all labels: $L \leftarrow \text{model.predict}(X)$
Reshape labels: $L \leftarrow \text{reshape}(L, \text{shape}(I))$
Compute cluster means: $\mu_i \leftarrow \text{mean}(I[L = i])$ for $i = 0, 1, \ldots, k - 1$
Find foreground cluster: $i_{fg} \leftarrow \arg\max_i \mu_i$
$B_{kmeans} \leftarrow (L = i_{fg})$                                ▷ Binary mask
return $B_{kmeans}$
```

Segmentation Combination

Algorithm 6 Combine Segmentation Results

```
Require: Binary images $B_{sauvola}$, $B_{kmeans}$
Ensure: Final binary image $B_{final}$
$B_{final} \leftarrow B_{sauvola} \vee B_{kmeans}$                  ▷ Logical OR operation
return $B_{final}$
```

Utility Functions

Algorithm 7 Utility Functions

```
procedure UniformFilter($I$, size)
    return Convolution of $I$ with uniform kernel of given size
end procedure
procedure BilinearInterpolate($G, y, x$)
    Compute weights and indices for 4 neighboring grid points
    return Weighted sum of neighboring values
end procedure
procedure RandomSample($X, n$)
    return $n$ randomly selected elements from $X$ without replacement
end procedure
```

Data availability

Data will be made available upon request.

References

[1] P. Iaccarino, E. Maresca, S. Morganti, F. Auricchio, E. Di Maio, Topologically optimized graded foams, Advanced Engineering Materials 26 (11) (2024) 2301798.

[2] B. Koohbor, S. Ravindran, A. Kidane, In situ deformation characterization of density-graded foams in quasi-static and impact loading conditions, International Journal of Impact Engineering 150 (2021) 103820.

[3] M. Smeets, B. Koohbor, G. Youssef, Quasi-static mechanical response of density-graded polyurea elastomeric foams, ACS Applied Polymer Materials 5 (4) (2023) 2840–2851.

[4] B. Koohbor, A. Kidane, Design optimization of continuously and discretely graded foam materials for efficient energy absorption, Materials & Design 102 (2016) 151–161.

[5] L. Gibson, M. Ashby, Cellular Solids, Structure and Properties - Second Edition, Cambridge University Press, 1997.

[6] H. Zhou, Y. Wang, X. Wang, Z. Zhao, G. Ma, Energy absorption of graded foam subjected to blast: a theoretical approach, Materials & Design 84 (2015) 351–358.

[7] M. Liang, Z. Li, F. Lu, X. Li, Theoretical and numerical investigation of blast responses of continuous-density graded cellular materials, Composite Structures 164 (2017) 170–179.

[8] D. Chen, S. Kitipornchai, J. Yang, Dynamic response and energy absorption of functionally graded porous structures, Materials & Design 140 (2018) 473–487.

[9] V. Gupta, A. Kidane, Designing density-graded cellular materials for tailored constitutive response, Composites Part B: Engineering 287 (2024) 111793.

[10] V. Gupta, A. Kidane, M. Sutton, Dynamic characteristics of density-graded cellular materials for impact mitigation, International Journal of Solids and Structures 296 (2024) 112816.

[11] Y. Ding, S. Wang, Z. Sun, V. Shim, Density-graded voronoi honeycombs–a local transversely isotropic description, International Journal of Solids and Structures 285 (2023) 112555.

[12] B. Chang, Z. Zheng, Y. Zhang, Y. Zhang, K. Zhao, J. Yu, Crashworthiness design of graded cellular materials: Experimental verification of the backward design strategy, International Journal of Impact Engineering 171 (2023) 104366.

[13] V. Gupta, A. Kidane, Impact response of additively manufactured density-graded open-cell foams, International Journal of Impact Engineering 195 (2025) 105127.

[14] M. Trofa, E. Di Maio, P. L. Maffettone, Multi-graded foams upon time-dependent exposition to blowing agent, Chemical Engineering Journal 362 (2019) 812–817.

[15] X. Zhu, Z. Cheng, Y. Chen, Thickness measurement of cell walls of closed-cell foams in micro-ct images, Journal of Microscopy 291 (2) (2023) 145–155.

[16] T. Ono, S. Samitsu, M. Hazutani, S. Ata, Structural characterization of hierarchical polymer foams by combining x-ray micro-computed tomography and scanning electron microscopy, Polymer Testing 140 (2024) 108580.

[17] D. S. Bolintineanu, R. Waymel, H. Collis, K. N. Long, E. C. Quintana, S. L. Kramer, Anisotropy evolution of elastomeric foams during uniaxial compression measured via in-situ x-ray computed tomography, Materialia 18 (2021) 101112.

[18] I. Koch, G. Preiß, M. Müller-Pabel, B. Grüber, M. Gude, Analysis of density-dependent cell structure of epp bead foams under compression, Experimental Mechanics (2025) 1–10.

[19] M. Foster, K. Steirer, J. Bernstein, M. Herynk, L. Lamberson, Influence of pore geometry and distribution on buckling under micro computed tomography, Polymer (2025) 128434.

[20] P. Cloetens, W. Ludwig, J. Baruchel, D. Van Dyck, J. Van Landuyt, J. Guigay, M. Schlenker, Holotomography: Quantitative phase tomography with micrometer resolution using hard synchrotron radiation x rays, Applied physics letters 75 (19) (1999) 2912–2914.

[21] J. Elliott, A. Windle, J. Hobdell, G. Eeckhaut, R. Oldman, W. Ludwig, E. Boller, P. Cloetens, J. Baruchel, In-situ deformation of an open-cell flexible polyurethane foam characterised by 3d computed microtomography, Journal of materials science 37 (2002) 1547–1555.

[22] S. Youssef, E. Maire, R. Gaertner, Finite element modelling of the actual structure of cellular materials determined by x-ray tomography, Acta materialia 53 (3) (2005) 719–730.

[23] J. Adrien, E. Maire, N. Gimenez, V. Sauvant-Moynot, Experimental study of the compression behaviour of syntactic foams by in situ x-ray tomography, Acta Materialia 55 (5) (2007) 1667–1679.

[24] S. Roux, F. Hild, P. Viot, D. Bernard, Three-dimensional image correlation from x-ray computed tomography of solid foam, Composites Part A: Applied science and manufacturing 39 (8) (2008) 1253–1265.

[25] H. Chai, H. Li, X. Xiao, J. Huang, S. Luo, Correlation between cell wall buckling and deformation banding in a closed-cell foam, Scripta Materialia 170 (2019) 177–182.

[26] H. Chai, Z. Xie, X. Xiao, H. Xie, J. Huang, S. Luo, Microstructural characterization and constitutive modeling of deformation of closed-cell foams based on in situ x-ray tomography, International Journal of Plasticity 131 (2020) 102730.

[27] L. Miele, E. Di Lorenzo, C. Guissart, E. Di Maio, Liquid foaming of tpu with methylal, Heliyon 10 (12) (2024).

[28] P. Iaccarino, P. Sisti, D. Ferri, E. Di Maio, Insights into the quasi-static mechanics of transversely isotropic polymer foams, Available at SSRN (2025). doi:http://dx.doi.org/10.2139/ssrn.5333828.

[29] R. Weast, Handbook of Chemistry and Physics 53rd Edition, Chemical Rubber Pub., 1972.
URL `https://books.google.it/books?id=aXHKtAEACAAJ`

[30] T. Weitkamp, M. Scheel, J. Giorgetta, V. Joyet, V. Le Roux, G. Cauchon, T. Moreno, F. Polack, A. Thompson, J. Samama, The tomography beamline ANATOMIX at Synchrotron SOLEIL, in: Journal of Physics: Conference Series, Vol. 849 (012037), IOP Publishing, 2017.

[31] T. Weitkamp, M. Scheel, J. Perrin, G. Daniel, A. King, V. Le Roux, J.-L. Giorgetta, A. Carcy, F. Langlois, K. Desjardins, et al., Microtomography on the ANATOMIX beamline at Synchrotron SOLEIL, in: Journal of Physics: Conference Series, Vol. 2380 (012122), IOP Publishing, 2022.

[32] J. Susini, J.-M. Cassagne, B. Gagey, A. Nadji, A. Taleb, A. Thompson, J. Daillant, A brief introduction to the Synchrotron SOLEIL and its upgrade programme, The European Physical Journal Plus 139 (1) (2024) 80.

[33] M. Pelerin, A. King, L. Laiarinandrasana, H. Proudhon, Development of a versatile mechanical testing device for in situ synchrotron tomography and diffraction experiments, Integrating Materials and Manufacturing Innovation 8 (2019) 378–387.

[34] A. King, N. Guignot, J.-P. Deslandes, M. Pelerin, I. Joosten, D. De Looff, J. Li, L. Bertrand, E. Rosenberg, A. Dewaele, et al., Recent tomographic imaging developments at the psiche beamline, Integrating Materials and Manufacturing Innovation 8 (4) (2019) 551–558.

[35] A. Mirone, E. Brun, E. Gouillart, P. Tafforeau, J. Kieffer, The pyhst2 hybrid distributed code for high speed tomographic reconstruction with iterative reconstruction and a priori knowledge capabilities, Nuclear Instruments and Methods in Physics Research Section B: Beam Interactions with Materials and Atoms 324 (2014) 41–48.

[36] P. Iaccarino, E. Di Maio, A. Constantinescu, F. Auricchio, Thermorheologically complex polymers: multiaxial constitutive modeling, numerical implementation and experimental validation, Polymer Testing 150 (2025) 108937.

[37] A. Greco, F. Lionetto, The influence of the stress relaxation and creep recovery times on the viscoelastic properties of open cell foams, Polymer Engineering & Science 49 (6) (2009) 1142–1150.

[38] A. K. Landauer, Z. Tsinas, O. L. Kafka, N. H. Moser, J. L. Glover, A. M. Forster, Unintended consequences: Assessing thermo-mechanical changes in vinyl nitrile foam due to micro-computed x-ray tomographic imaging, Materials & design 235 (2023) 112381.

[39] J. Schindelin, I. Arganda-Carreras, E. Frise, V. Kaynig, M. Longair, T. Pietzsch, S. Preibisch, C. Rueden, S. Saalfeld, B. Schmid, et al., Fiji: an open-source platform for biological-image analysis, Nature methods 9 (7) (2012) 676–682.

[40] P. Virtanen, R. Gommers, T. E. Oliphant, M. Haberland, T. Reddy, D. Cournapeau, E. Burovski, P. Peterson, W. Weckesser, J. Bright, S. J. van der Walt, M. Brett, J. Wilson, K. J. Millman, N. Mayorov, A. R. J. Nelson, E. Jones, R. Kern, E. Larson, C. J. Carey, İ. Polat, Y. Feng, E. W. Moore, J. VanderPlas, D. Laxalde, J. Perktold, R. Cimrman, I. Henriksen, E. A. Quintero, C. R. Harris, A. M. Archibald, A. H. Ribeiro, F. Pedregosa, P. van Mulbregt, SciPy 1.0 Contributors, SciPy 1.0: Fundamental Algorithms for Scientific Computing in Python, Nature Methods 17 (2020) 261–272. doi:10.1038/s41592-019-0686-2.

[41] M. Avalle, G. Belingardi, R. Montanini, Characterization of polymeric structural foams under compressive impact loading by means of energy-absorption diagram, International journal of impact engineering 25 (5) (2001) 455–472.